JOURNAL OF SYNCHROTRON RADIATION

ISSN 1600-5775

Received 1 November 2016
Accepted 28 February 2017

Edited by G. E. Ice, Oak Ridge National Laboratory, USA

Keywords: Fresnel zone plate; X-ray microscopy; apodization; Gaussian beam optics.

Fresnel zone plate with apodized aperture for hard X-ray Gaussian beam optics

Akihisa Takeuchi,[a]* Kentaro Uesugi,[a] Yoshio Suzuki,[a,b] Seiichi Itabashi[c] and Masatoshi Oda[c,d]

[a]Japan Synchrotron Radiation Research Institute/SPring-8, Sayo, Hyogo 679-5198, Japan, [b]Graduate School of Frontier Sciences, University of Tokyo, Kashiwa, Chiba 277-8561, Japan, [c]NTT Advanced Technology, Atsugi, Kanagawa 243-0124, Japan, and [d]Aichi Science and Technology Foundation, Aichi Synchrotron Radiation Center, Seto, Aichi 489-0965, Japan. *Correspondence e-mail: take@spring8.or.jp

Fresnel zone plates with apodized apertures [apodization FZPs (A-FZPs)] have been developed to realise Gaussian beam optics in the hard X-ray region. The designed zone depth of A-FZPs gradually decreases from the center to peripheral regions. Such a zone structure forms a Gaussian-like smooth-shouldered aperture function which optically behaves as an apodization filter and produces a Gaussian-like focusing spot profile. Optical properties of two types of A-FZP, *i.e.* a circular type and a one-dimensional type, have been evaluated by using a microbeam knife-edge scan test, and have been carefully compared with those of normal FZP optics. Advantages of using A-FZPs are introduced.

1. Introduction

Fresnel zone plates (FZPs) are one of the most popular X-ray optical devices, for the following reasons: they have superior optical characteristics such as high spatial resolution up to several tens of nanometers (Chao *et al.*, 2012; Chen *et al.*, 2011; Suzuki *et al.*, 2010*a*; Takeuchi *et al.*, 2015; Takano *et al.*, 2010; Döring *et al.*, 2013), they are easy to align, and they are commercially obtainable ideal devices. Using several kinds of FZPs we have developed several kinds of hard X-ray microscope/tomography systems at the large synchrotron radiation facility SPring-8 (Takeuchi *et al.*, 2012, 2013), such as a scanning X-ray microscope (Takeuchi *et al.*, 2010), an imaging (full-field) X-ray microscope (Takeuchi *et al.*, 2002, 2006; Uesugi *et al.*, 2006), and a combination of these two optics called a scanning–imaging X-ray microscope (SIXM). They are now widely used for various kinds of applications (Toda *et al.*, 2006; Tsuchiyama *et al.*, 2011; Mizutani *et al.*, 2013).

Although they have enabled high-spatial-resolution non-destructive three-dimensional observations, some optical problems still remain in imaging microscope optics. These include a kind of false image contrast due to edge-enhanced contrast and periodic fringe patterns known as ringing (Takeuchi *et al.*, 2013). They are seen along a surface or an interface of an object, even in the on-focus condition. They obviously decrease the image quality and make it difficult for the quantitative interpretation of image contrast. An effective method of reducing the edge-enhancement and ringing is to employ Gaussian beam optics. For focusing beam optics, it is well known that Gaussian beam optics enable a Gaussian-like focused beam to be produced without side lobes, unlike the Bessel function.

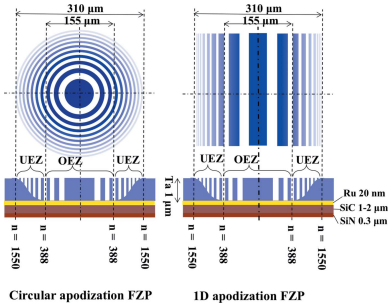

Gaussian beam optics can be realised in two ways. One way is to install a spatial filter in the focal plane to eliminate side lobes of the diffraction-limited focused beam. In the hard X-ray region, some attempts have already been proposed. Speckle-free X-ray Gabor holography with a spherical wave has been performed using focused optics and a spatial filter in the focal plane (Suzuki *et al.*, 2010*b*; Suzuki & Takeuchi, 2012). Apodized illumination X-ray coherent diffraction imaging (CDI) using a focused beam and a spatial filter has been suggested for observing spatially extended objects which have not been observable by conventional CDI (Kimura *et al.*, 2013; Khakurel *et al.*, 2015). However, this method, which requires diffraction-limited focusing optics with a coherent beam, is not feasible for imaging microscope optics. The other way to realise Gaussian beam optics is to install an apodization filter at the pupil of the optical device to make a smooth-shouldered (Gaussian-like) pupil function, that is applicable also for imaging microscope optics. The apodization filter gradually reduces the intensity of the transmitted light from the central to the peripheral regions of the pupil without phase perturbation. In the visible-light region, a radially graduated neutral density filter is used as an apodization filter. In the X-ray region, however, where all the materials have some amount of attenuation and phase shift, an effective absorption-type apodization filter is not available. Although photon sieves and modified FZPs utilizing the idea of a photon sieve have been proposed to produce Gaussian beam optics by controlling the density of large numbers of opening apertures on a perfectly opaque material (Cao & Jahns, 2003; Yang, 1993), these devices are only applicable in the soft X-ray region where the penetrating power is small. In the hard X-ray region, phase modulation must be taken into account as well as absorption. For example, X-ray refractive lenses themselves natively have an apodization function because their transmittance gradually decreases from the axial center to the peripheral regions of the aperture (Kipp *et al.*, 2001). In the case of FZPs, most of the devices fabricated by the lithography technique are phase-type in the hard X-ray region. Therefore, apodization should be realised by modifying the zone structures in order to produce a gradually decreasing diffraction efficiency from the center to the outer regions. We have developed FZPs with apodization functions, called apodization FZPs (A-FZPs). In this paper, details of these A-FZPs will be presented, and their optical properties evaluated using X-ray microbeam optics, and carefully compared with those of conventional FZPs.

2. Apodization FZP

In actual use in the hard X-ray region, FZPs often unintentionally have a kind of apodization effect on the device, due to a gradual decrease of the diffraction efficiency distribution along the radius of the zone plate. This decrease is caused by a fabrication error in the FZP pattern that is generally more noticeable in the outermost regions (Takeuchi *et al.*, 2015; Suzuki *et al.*, 2005). This means that a FZP with an apodized aperture can be fabricated by validly utilizing such a 'shape error'. Diffraction efficiency can be controlled

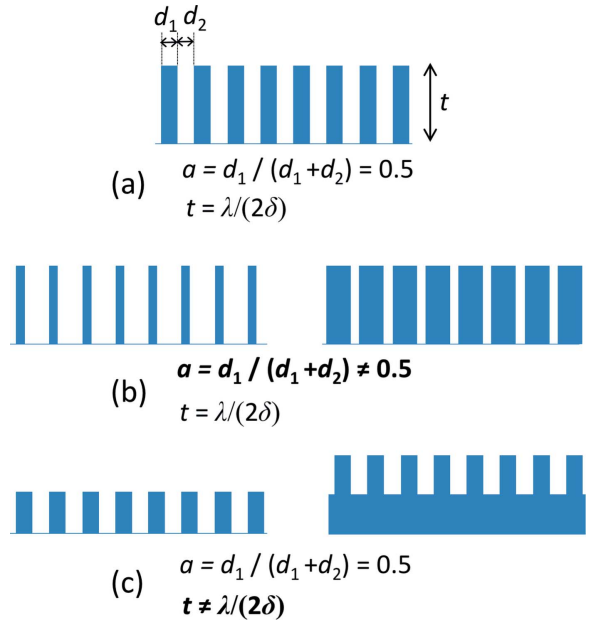

Figure 1
Types of shape error of grating (zone) structures: (*a*) ideal structure to realise a maximum diffraction efficiency, satisfying $a = 0.5$ and $t = \lambda/(2\delta)$, where a is the zone ratio defined as $a = d_1/(d_1 + d_2)$, d_1 and d_2 are the widths of the opaque and transmitting zones, respectively, t is the zone thickness, λ is the wavelength and δ is the decrement of the refraction index from unity; (*b*) zone ratio $a \neq 0.5$, (*c*) zone thickness $t \neq \lambda/(2\delta)$.

(reduced) in two ways: either by changing the zone ratios of opaque and transmitting zones from 1:1 [as shown in Fig. 1(*b*), where Fig. 1(*a*) shows an ideal shape], or by changing the zone thicknesses [Fig. 1(*c*)]. The diffraction efficiency of the mth order, ε_m, with a zone thickness of t is expressed by kinematic diffraction theory, as

$$\varepsilon_m = \begin{cases} \dfrac{1-\cos(2\pi m a)}{2\pi^2 m^2}\left\{1+\exp[-(4\pi/\lambda)\beta t]\right. & m \neq 0, \\ \left. -2\exp[-(2\pi/\lambda)\beta t]\cos[(2\pi/\lambda)\delta t]\right\}, & \\ a^2 + (a-1)^2\exp[-(4\pi/\lambda)\beta t] & m = 0, \\ -2a(a-1)\exp[-(2\pi/\lambda)\beta t]\cos[(2\pi/\lambda)\delta t], & \end{cases} \quad (1)$$

where a is the zone ratio defined as [opaque zone width]/[zone pitch], λ is the wavelength, β is the imaginary part of the refractive index and δ is the refractive index decrement from unity. Fig. 2(*a*) shows the relationship between the diffraction efficiencies calculated by equation (1) and the zone ratio, representing the case of Fig. 1(*b*). The diffraction efficiency of the first order becomes maximum when the zone ratio a is 0.5 (opaque zone width d_1:transmit zone width d_2 = 1:1) and decreases as the zone ratio moves away from 0.5 with an increase of the efficiency of the other diffraction orders. Therefore, the apodization function may be realised by employing a zone structure that gradually changes the zone ratio from 0.5 in the central region to 1 (or 0) in the peripheral regions. Fig. 2(*b*) shows an example of the relationship between the calculated diffraction efficiencies and the zone

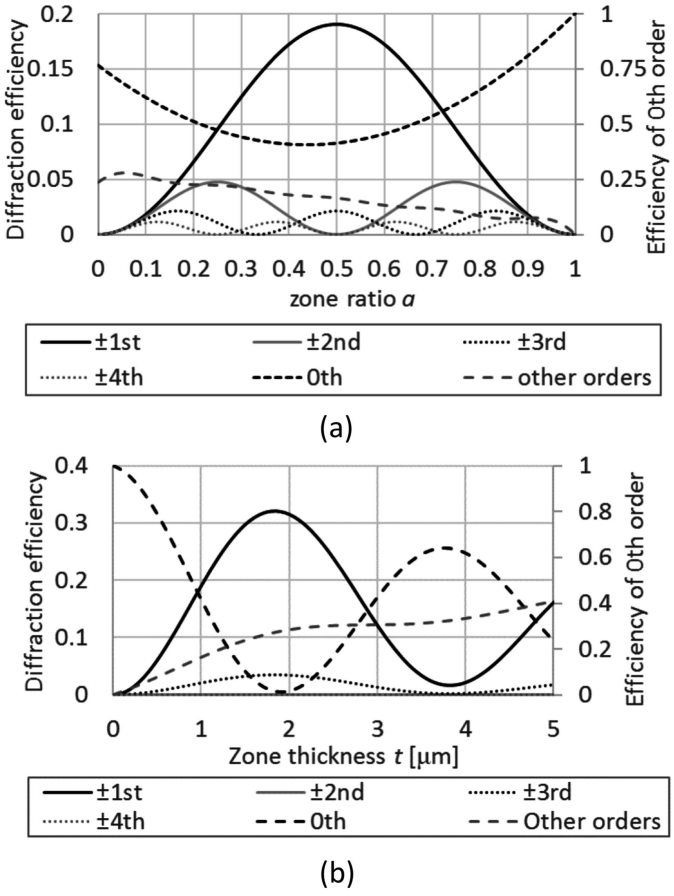

Figure 2
Relationship between the diffraction efficiencies (0th, ±1st, ±2nd, ±3rd, ±4th and other orders) and the zone structures: (*a*) zone ratio *a*, and (*b*) zone thickness *t*. The supposed X-ray energy is 8 keV and the zone material is tantalum ($\beta = 3.30 \times 10^{-5}$, $\delta = 4.03 \times 10^{-5}$).

thickness, representing the case of Fig. 1(*c*). The first-order diffraction efficiency of a phase-type FZP becomes maximum with a zone thickness that makes a half-wavelength phase shift, corresponding to a thickness of 1.92 μm of tantalum for 8 keV X-rays (the exact maximum of the first-order diffraction is at 1.84 μm because of the absorption of tantalum). Actually, most FZPs fabricated by the lithography technique have a half-wavelength phase shift or smaller in the hard X-ray region, because manufacturable zone thicknesses are technically restricted to be smaller than several micrometers. In this case, the relationship between the zone thickness and the efficiency of the first-order diffraction can be regarded as a monotonic increase. Therefore, zone structures with radially decreasing zone thickness from the center to the peripheral regions will result in a radially decreasing efficiency distribution that will realise an apodization function.

Of the above-mentioned two types of apodization FZPs, we have decided to employ the latter type, shown in Fig. 1(*c*). With regard to how to fabricate a graduated zone thickness structure by electron-beam lithography and reactive ion etching techniques, fortunately there is a suitable effect in the reactive ion etching process called the 'micro-loading effect'. This effect is an inherent phenomenon observed in the process such that the etching rate decreases with the reduction of the pattern width (Oda *et al.*, 1993; Ozawa *et al.*, 1997). This effect is more remarkable for fine structures, and causes non-uniformity of the etching depth between wide and narrow patterns. While this effect was originally a serious problem for the fabrication of even thicknesses, it can be turned into an advantage for producing apodization naturally. A gradually decreasing zone thickness [whereas wide zone patterns in the central region have an ideal zone depth shown in Fig. 1(*a*), narrow patterns in the outer regions have an insufficient zone depth shown on the right of Fig. 1(*c*)] can be realised by validly utilizing the 'micro-loading effect'.

Conceptual drawings of an A-FZP are shown in Fig. 3 along with a conventional FZP for comparison. Cross sections of their aperture function corresponding to the diffraction efficiency distributions are also shown in Figs. 3(*c*) and 3(*c*′). The zone thickness of an 'ideal' conventional FZP is even, as shown in Fig. 3(*b*′). On the other hand, that of the A-FZP is not even, but decreases toward the outermost regions, as shown in Figs. 3(*b*-1) and 3(*b*-2). Both of these two zone structures have the effect of a 'phase-type' apodization filter in the hard X-ray region, and the structure shown in Fig. 3(*b*-2) can be fabricated using the micro-loading effect. Because the diffraction efficiency is determined by the zone thickness, the aperture function of an A-FZP has a smooth-shouldered shape like a Gaussian [Fig. 3(*c*)], whereas that of a conventional FZP is rectangular [Fig. 3(*c*′)]. Their respective point-spread functions (PSFs) are shown in Figs. 3(*d*) and 3(*d*′). The expected focused beam profile might be Gaussian-like with slight side peaks, whereas that of a conventional FZP is known to be a square of the Bessel function (or sinc function in the case of one-dimensional focusing) with side lobes.

A-FZPs fabricated by lithography techniques have extraneous advantages besides Gaussian beam optics. The diffrac-

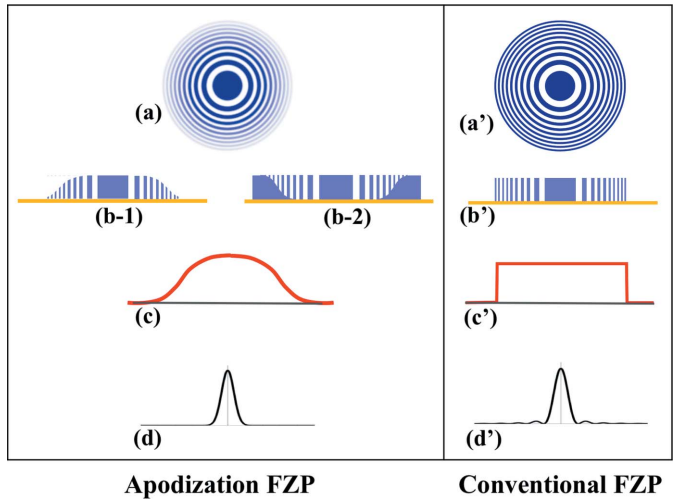

Figure 3
Conceptual drawings of the apodization FZP (left) and the conventional FZP for comparison (right). Top views (*a* and *a*′), cross-sectional views (*b*-1, *b*-2, and *b*′), cross sections of the aperture function corresponding to the distribution of first-order diffraction efficiency (*c* and *c*′), and their respective point-spread functions (*d* and *d*′).

tion-limited spatial resolution of FZP optics is determined by the outermost zone width; and the diffraction efficiency is determined by the thickness of the zone structure. Therefore, in the hard X-ray region, the aspect ratio, defined as the ratio between the zone thickness and the outermost zone width, is required to be as high as possible. In general, however, the aspect ratio of FZPs fabricated by lithography techniques is technically restricted to be lower than about 10. Therefore, the appropriate X-ray energy range and the spatial resolution are actually determined by such a technical restriction. For example, the appropriate X-ray energy range for a Ta FZP of thickness 1 μm is approximately below the Ta *L*-edge of 9.8 keV, and the efficiency becomes maximum at 5.3 keV (32%). However, the spatial resolution is technically restricted to be approximately 100 nm by the aspect ratio of the zone pattern. Therefore, optical characteristics of the FZP are strictly restricted by the aspect ratio. On the other hand, in the case of A-FZPs in which the thicknesses of the outer zones are allowed to be smaller than those of the inner zones, such a restriction is immediately relaxed. The following optical characteristics, compared with conventional FZPs, are available:

(1) A large numerical aperture (NA); high spatial resolution and high correcting efficiency, large diameter; large field of view of the imaging microscope.

(2) A thick inner zone; high efficiency/use in the high X-ray energy region.

Figs. 4(*a*) and 4(*b*) show a comparison between a conventional FZP and an A-FZP with the same zone thickness t in the central region. The manufactural outermost zone width Δr_N of the conventional FZP with zone number N is technically restricted by the condition $t/\Delta r_N \simeq 10$. On the other hand, the structure of an A-FZP can be assumed to be the combination of a conventional FZP with an outermost zone width of Δr_N and additional zones with gradually decreasing zone thickness located outside of the Nth zone as shown in Fig. 4(*b*). As a result, this A-FZP has a larger NA than a conventional one. Moreover, the correction efficiency, defined as a product of the diffraction efficiency distribution and the solid angle of the aperture, also increases because of the additional zone regions (the averaged diffraction efficiency decreases). Also, a larger diameter of the FZP as an objective widens the field of view of imaging microscope optics.

On the contrary, A-FZPs also make it easy to realise a higher diffraction efficiency than conventional FZPs. Figs. 4(*a*) and 4(*c*) show a comparison between a conventional FZP and another type of A-FZP. In this case, both the thickness and width of the outermost zones of these two optics are the same, but the zone thickness of the center region of the A-FZP is larger than that of the conventional FZP. Therefore, a higher efficiency in the higher X-ray energy region is available without extreme loss of spatial resolution. As described here, two-types of A-FZP are available: the former is a high-spatial-resolution type, and the latter is a high-efficiency type, compared with the basic conventional FZP. Moreover, the coexististence of both high resolution and high efficiency is available by combining these two types of FZP [Fig. 4(*d*)].

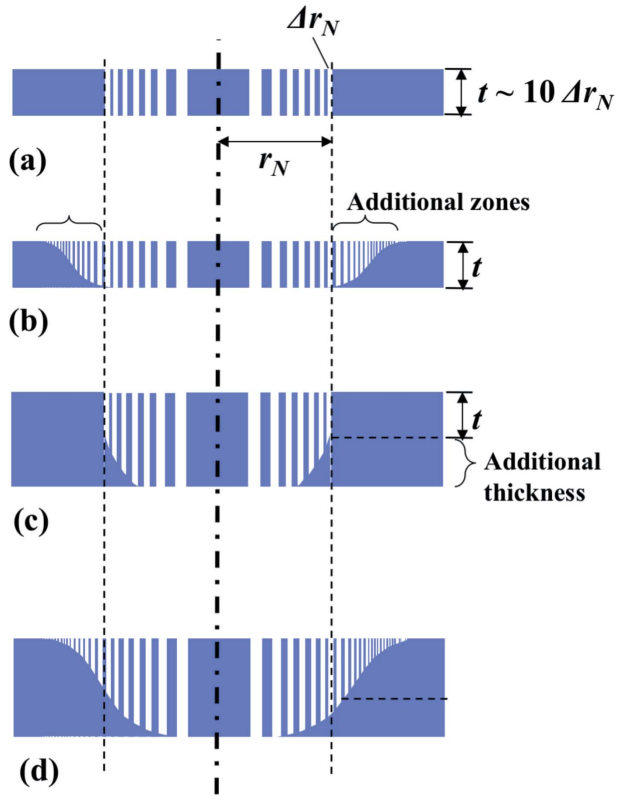

Figure 4
Comparison between (*a*) a conventional FZP, (*b*) an A-FZP of the same thickness t (high-resolution type), (*c*) an A-FZP with the same outermost zone width Δr_N (high-efficiency type), and (*d*) high-resolution and high-efficiency type.

A circular A-FZP for two-dimensional imaging and a one-dimensional (1D) A-FZP used as a 1D optical device for SIXM have been fabricated. Schematic diagrams of the A-FZPs are shown in Fig. 5, and designed parameters of the A-FZPs are shown in Table 1. Parameters of conventional FZPs used as a basic design for A-FZPs are also shown for comparison. All of the FZPs used in these experiments were fabricated by NTT-AT. In the fabrication of conventional FZPs, where the effect of micro-loading must be reduced as much as possible, most zones are over-etched so that the outermost zone is completely etched. On the other hand, in the case of the A-FZP, etching is stopped before completion. Therefore, the outer zones are partially etched whereas the inner zones are over-etched. Except for this etching condition though, the fabrication process for the A-FZP is almost the same as that of the conventional FZP. Details of the fabrication process of the FZP are expressed elsewhere (Suzuki *et al.*, 2010*a*; Ozawa *et al.*, 1997; Sekimoto *et al.*, 1998). Compared with a conventional (basic) FZP of type 1 in Table 1, fabricated A-FZPs are assumed to be high-resolution types, which are designed by adding outer zones to the basic FZP. The parameters of the inner-half of the A-FZP are just the same as those of the basic FZP of type 1. Each FZP pattern was drawn on a three-layered membrane consisting of Ru 20 nm, SiC 1–2 μm and SiN 0.3 μm. The material of the FZP is tantalum, of thickness 1 μm. The width of the A-FZP pattern

Table 1
Typical parameters of apodization FZPs and conventional FZPs fabricated by the e-beam lithography method at NTT-AT. In the experiment, the effective zone thicknesses of 1D FZPs are twice the shown values by inclining the FZP devices to 60°.

FZP type		Apodization FZP	Basic (conventional) FZP	
			Type 1	Type 2
Base plate		Si 10 mm × 10 mm × 0.625 mm		
Membrane		Ru 20 nm/SiC 2 mm/SiN 0.3 mm		
Zone material		Ta		
Outermost zone width		50 nm	100 nm	50 nm
Zone number		1550	388	1550
Total length of FZP patterns		310 µm	155 µm	310 µm
Zone thickness	Inner-half region	1 µm	1 µm	0.5 µm
	Outer-half region	Determined by micro-loading effect		

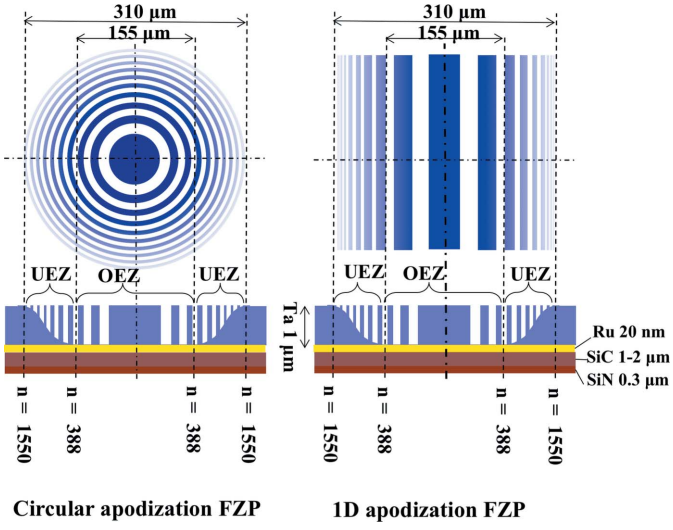

Figure 5
Schematic diagram (not in scale) of a fabricated circular A-FZP (left) and a 1D A-FZP (right). Top: top view. Bottom: cross-sectional view. OEZ: over-etched zones. UEZ: under-etched zones. The etching condition was optimized so that the 388th zone might be just 1 µm thick. Therefore, inner zones than the 387th zone are over-etched resulting in an even zone thickness of 1 µm, and outer zones are under-etched resulting in a gradually decreasing zone thickness due to the micro-loading effect.

is 310 µm, the number of zones N is 1540 and the outermost zone width Δr_N is 50 nm. The focal length at an X-ray energy of 8 keV is 100 mm. The designed zone depth of the region between the center and the 388th zone corresponding to a zone width of 100 nm is 1 µm, and that of the outer region from the 389th zone to the outermost zone is gradually decreasing. Therefore, the inner 388 zones were completely etched as well as the conventional FZP, while the thicknesses of the outer 1162 zones were determined by the micro-loading effect of the dry-etching process.

3. Experimental procedure

Optical performance tests of a circular A-FZP and a 1D A-FZP have been carried out at the undulator beamline 20XU of SPring-8 (Suzuki *et al.*, 2004). Focused beam profiles for coherent hard X-rays were precisely measured using knife-edge scan tests with differential phase contrast configurations (Takeuchi *et al.*, 2015). The experimental setup is shown in Fig. 6. An X-ray energy of 8 keV was chosen by passing through a liquid-nitrogen-cooled silicon 111 double-crystal monochromator. The energy resolution of the used beam was about ΔE = 1.1 eV for E = 8 keV. The monochromaticity of $\Delta E/E$ = 1.1/8000 was sufficient to avoid chromatic aberration of the FZPs used (numbers of zones N = 1550 at maximum). A precise cross slit with an opening of 50 µm × 50 µm located 49 m from the source was used as a pseudo source for determining the spatial coherence at the experimental station. An X-ray beam was transported through a vacuum duct, and was extracted into air at an experimental station located approximately 245 m from the source. A silicon nitride film of thickness 10 µm was used as a vacuum window. Therefore, the geometrical spot size for the FZP with a focal length of 100 mm was approximately 25.5 nm. The patterned edge of a tantalum resolution test chart (NTT-AT ATN/XRESO-50HC) with a thickness of 0.5 µm was used as a knife-edge. A stepping-motor-driven mechanical stage (Kohzu Precision YA-05-14) with a measured accuracy of better than 10 nm was used as a translation scan stage for the knife-edge (Suzuki *et al.*, 2001). As for the order-sorting aperture, a platinum pinhole with an opening diameter of 20 µm and a tantalum slit with an opening width of 20 µm were used for the circular FZPs and 1D FZPs, respectively. A scientific complementary metal-oxide-semiconductor (sCMOS) imaging sensor (Hamamatsu Photonics C11440-22CU) with a visible-light conversion unit consisting of a P43 (Gd2O2S:Tb powder, 20 µm thickness) scintillator and optical relay lenses was used as a multipixel detector for the differential-phase-contrast measurement for the knife-edge scan. The effective pixel size was 6.5 µm, and the pixel format was 2048 × 2048. The distance between the knife-edge and the detector was 160 mm. In the SIXM experiments where 1D FZPs are used, 1D FZPs are set inclined in the plane perpendicular to the zone direction by 60° to increase the effective zone thickness for the purpose of maximizing the

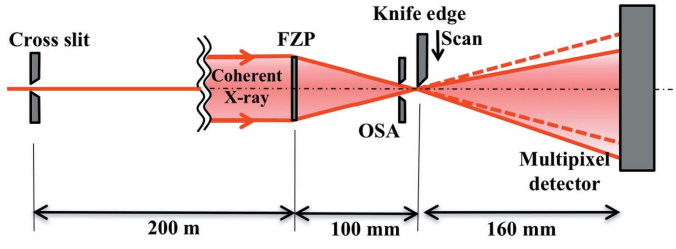

Figure 6
Experimental setup of the microbeam experiment at BL20XU at SPring-8 (top view). The undulator light source and double-crystal monochromator are omitted. FZP: circular FZP, circular A-FZP, 1D FZP and 1D A-FZP with the same focal length of 100 mm were installed one after another. OSA: order-sorting aperture (platinum pinhole with diameter of 20 µm for circular FZPs, tantalum slit with 20 µm width for 1D FZPs). A cross slit with an opening width of 50 µm × 50 µm is used for defining the effective X-ray source size.

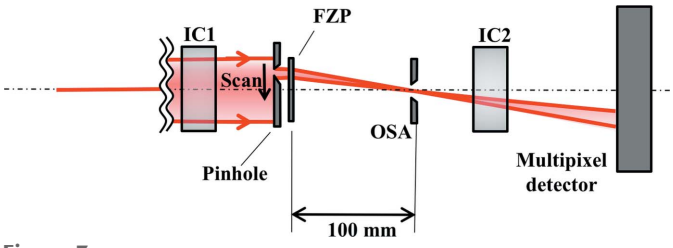

Figure 7
Experimental setup for measurement of the first-order diffraction efficiency distribution of the FZPs (top view). The undulator light source, double-crystal monochromator and cross slit as a pseudo source are omitted. IC1 and IC2: ionization chambers. A platinum pinhole with an opening size of 10 µm was used for scanning. FZP: circular FZP, circular A-FZP, 1D FZP and 1D A-FZPs with the same focal length of 100 mm were installed one after another. OSA: order-sorting aperture (platinum pinhole with diameter of 20 µm for circular FZPs, tantalum slit with 20 µm width for 1D FZPs).

diffraction efficiency at 8 keV (Takeuchi *et al.*, 2012). Therefore, also in this experiment, 1D FZPs were set inclined by 60° for evaluation under the actual conditions used. Conventional-type FZPs (type 1 in Table 1) were also evaluated under the same experimental conditions. The experimental results for A-FZPs were carefully compared with those of the conventional FZPs. Regional efficiency distributions of the first-order diffraction of the A-FZPs were measured by scanning a platinum pinhole with opening diameter of 10 µm additionally installed just in front of the FZP (Fig. 7).

4. Results and discussion

4.1. Focused beam profile

Measured focusing beam profiles of a circular A-FZP and a conventional circular FZP are shown in Fig. 8. Focused beam sizes were 65 nm and 124 nm full width at half-maximum (FWHM), respectively. Focused beam profiles of a 1D A-FZP and of a conventional 1D FZP are shown in Fig. 9. Measured beam spot sizes were 55 nm and 98 nm FWHM, respectively. All of these four profiles show nearly diffraction-limited focusing. By employing A-FZPs with twice the NA compared with conventional FZPs, focused beams with a half-width have been successfully obtained.

Figs. 10 and 11 show vertically magnified views of the focused beam profile of Figs. 8 and 9, respectively. The measured focusing profile of the conventional FZP (type 1) with a circular aperture is shown as a black line in Fig. 10(*b*). A knife-edge scan profile represents a line-spread function (LSF). Therefore, for comparison, theoretical values of the LSF, expressed as

$$\mathrm{LSF}(x) = \int \left[2J_1\left(\pi r/\Delta r_N\right)\Big/\left(\pi r/\Delta r_N\right)\right]^2 \mathrm{d}y \qquad (2)$$

where J_1 is the Bessel function of the first kind and r is the distance around the optical axis, $r = (x^2 + y^2)^{1/2}$, are shown as gray lines in Fig. 10. In the conventional FZP focusing shown

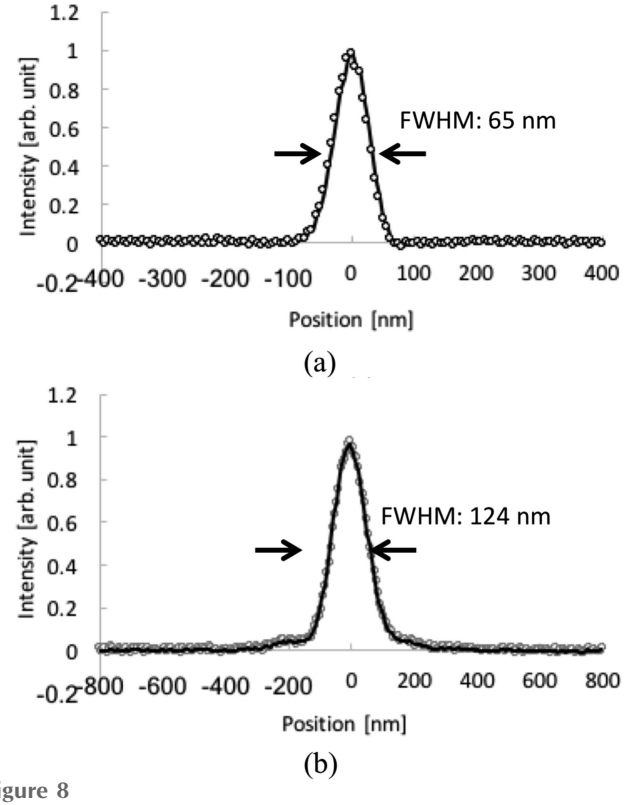

Figure 8
Focused beam profiles of circular FZPs measured with the differential-phase-contrast knife-edge scan test. Open circles represent the scan data, black lines represent the moving averages of three scan points. (*a*) Apodization FZP. (*b*) Conventional FZP. The scan step was 6.25 nm, the dwell time was 0.1 s and the X-ray energy was 8 keV.

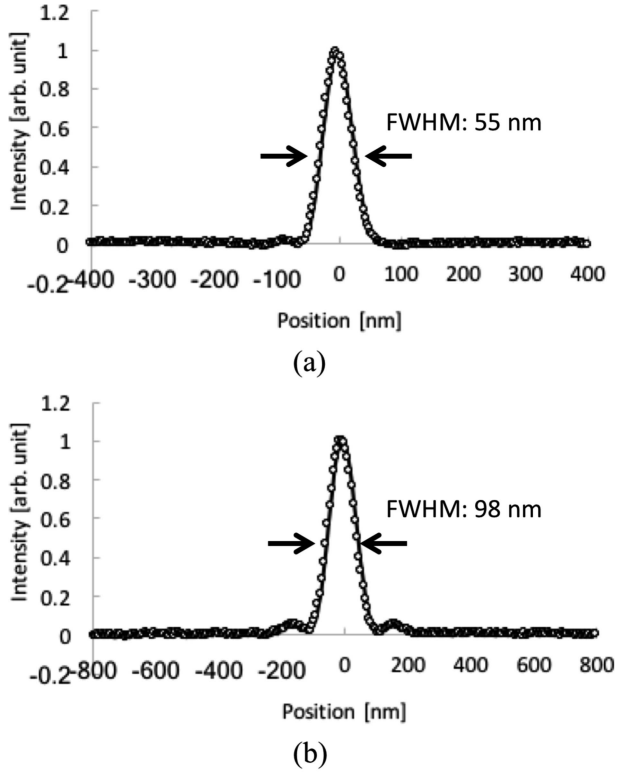

Figure 9
Focused beam profiles of 1D FZPs measured using the differential-phase-contrast knife-edge scan test. Open circles represent the scan data, black lines represent the moving averages of three scan points. (*a*) Apodization FZP, scan step 3.125 nm, and (*b*) conventional FZP, scan step 6.25 nm. The dwell time was 0.1 s and the X-ray energy was 8 keV.

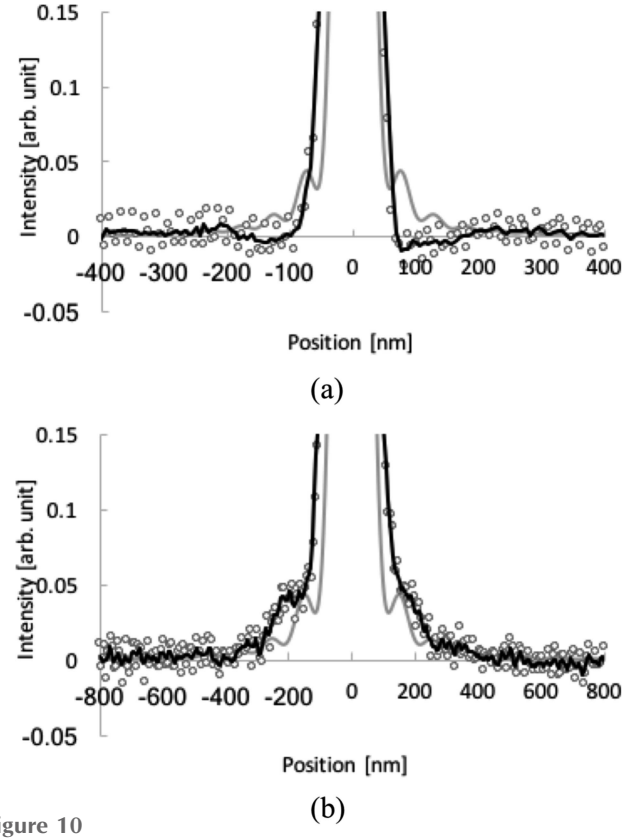

Figure 10
Magnified views of the focused beam profiles of Fig. 8. (*a*) Apodization FZP, (*b*) conventional FZP. Open circles represent the scan data, black lines represent the moving averages of three scan points. Theoretical LSFs of a conventional FZP are shown as gray lines for comparison.

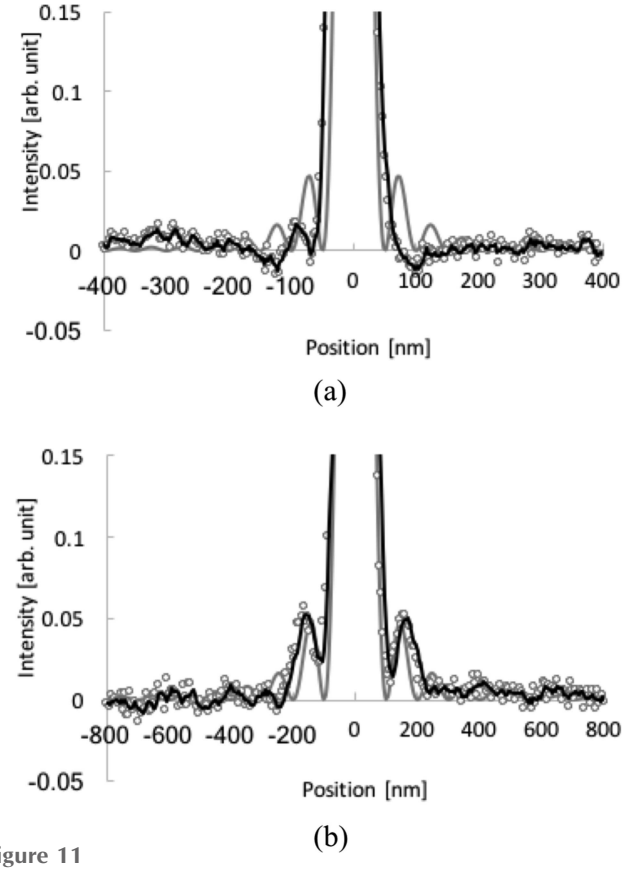

Figure 11
Magnified views of the focused beam profiles of Fig. 9. (*a*) Apodization FZP, (*b*) conventional FZP. Open circles represent the scan data, black lines represent the moving averages of three scan points. Theoretical LSFs of a conventional FZP are shown as gray lines for comparison.

in Fig. 10(*b*), although the measured profile has gentle side shoulders without the first minimum, side lobes of the second maximum are clearly recognized. The intensity ratio between the second maximum and the main peak is approximately 0.05, which shows good agreement with the theoretical value of a LSF of a circular aperture optics (0.057). On the other hand, almost no side lobe (below the noise level) is recognized in the A-FZP focusing as shown in Fig. 10(*a*).

Fig. 11(*b*) shows the measured focusing profile of the conventional 1D FZP (type 1). LSFs for 1D focusing with a rectangular aperture correspond to the square of the sinc function,

$$\mathrm{LSF}(x) = \left[\frac{\sin(\pi x/\Delta r_N)}{(\pi x/\Delta r_N)}\right]^2, \qquad (3)$$

shown as gray lines in Fig. 11. The relative intensity of its first minimum is zero, and that of the second maximum is 0.047. The measured profile in Fig. 11(*b*) clearly shows both of them, and the intensity ratio between the second maximum and the main peak is approximately 0.05, showing a good agreement with the theoretical value. On the other hand, such a subsidiary maximum is hardly observed in the A-FZP focusing shown in Fig. 11(*a*).

These results clearly show that Gaussian-like focusing profiles with only a main peak have been successfully realised using the A-FZP optics.

4.2. Efficiency

Fig. 12 shows a two-dimensional distribution and its cross-sectional profile of the first-order diffraction efficiency of the circular A-FZP. The X-ray energy is 8 keV. The efficiency distribution gradually drops from the inner region to the outer region. The efficiencies in the vicinity of the central and the outermost regions are 0.16 and 0.05, respectively. The measured total efficiency of the first-order diffraction is 0.09. On the other hand, the theoretical value defined in equation (1) is 0.19 for a tantalum FZP with a zone thickness of 1 µm.

Fig. 13 shows the distribution of the first-order diffraction efficiency of a 1D A-FZP. The efficiency distribution shows a gentle slope from 0.28 in the vicinity of the center to 0.11 in the peripheral regions of the zone plate pattern. The total efficiency of the first-order diffraction was measured to be 0.23, whereas the theoretical value of the FZP with zone thickness of 2 µm is 0.32.

The discrepancies between the measured and the theoretical values of the total efficiency are due to the gradual decrease of the diffraction efficiency. Although such a

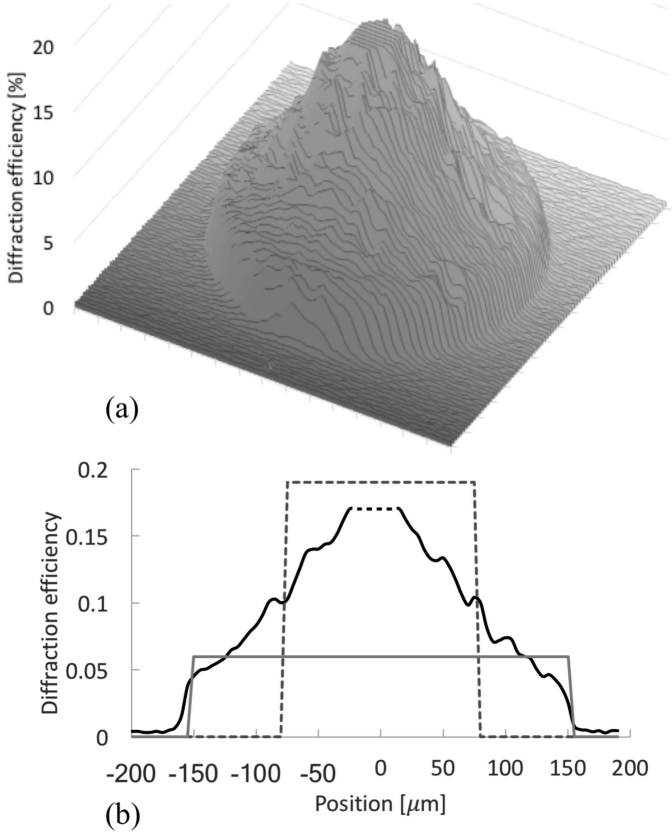

Figure 12
Efficiency distribution of the first-order diffraction of a circular A-FZP. (*a*) Bird's-eye view of the two-dimensional distribution and (*b*) cross-sectional profile (black solid line). The central region including the zeroth-order beam is cut. The X-ray energy is 8 keV. Theoretical values of conventional FZPs are also shown (gray broken line: outermost zone width is 100 nm and zone thickness is 1 μm; gray solid line: outermost zone width is 50 nm and zone thickness is 0.5 μm). Small bumps shown in the profile are due to the speckle from the dust adhered on the windows installed in the X-ray path.

decrease of the diffraction efficiency causes a reduction of the signal, the correction efficiencies are still larger than the basic conventional FZPs because of the two times larger NA. The theoretical distribution of the diffraction efficiency of the conventional FZP with the same zone thickness (type 1 in Table 1) is shown in Figs. 12 and 13 as gray broken lines. The correcting efficiency of 1D FZPs is defined as the integral of the efficiency profile, and that of circular FZPs is defined as the volume of the rotating body of the profile around the optical axis. Compared with conventional FZPs, circular-type and 1D-type A-FZPs have approximately 2 times and 1.4 times the correction efficiencies, respectively. Next, let us compare A-FZPs with other conventional FZPs having the same NA (type 2 in Table 1). In this case, the effective zone thickness of the conventional circular FZPs is restricted to 0.5 μm, and that of the 1D FZP is 1 μm by inclining by 60°. Their diffraction efficiency distributions are shown in Figs. 12 and 13 as gray lines. Compared with the theoretical values of these FZPs, circular-type and 1D-type A-FZPs have approximately 1.8 times and 1.2 times larger correcting efficiencies, respectively. Therefore, these results show that

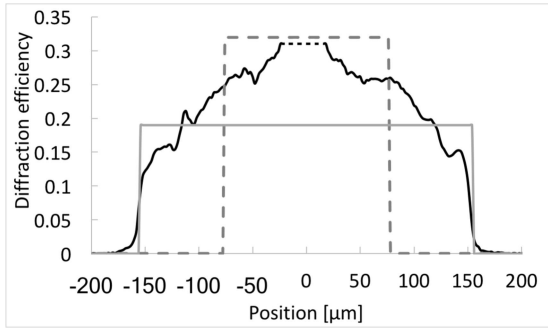

Figure 13
Efficiency distribution of the first-order diffraction of a 1D A-FZP (black solid line). The central region including zeroth-order beam is cut. The X-ray energy is 8 keV. Theoretical values of conventional FZPs are also shown (gray broken line: outermost zone width is 100 nm and zone thickness is 2 μm; gray solid line: outermost zone width is 50 nm and zone thickness is 1 μm). Small bumps shown in the profile are due to the speckle from the dust adhered on the windows installed in the X-ray path.

A-FZPs realise larger correction efficiencies than conventional FZPs.

5. Conclusion

FZPs with an apodization aperture (A-FZPs) X-ray optics have been developed to realise Gaussian beam by validly utilizing a micro-loading effect which causes dependencies of dry-etching speed on the pattern width. The focusing properties of a circular A-FZP and a 1D A-FZP have been evaluated by knife-edge scan tests. Nearly diffraction-limited Gaussian-like focused beam profiles without side lobes were successfully obtained. Distributions of the first-order diffraction efficiencies have been measured. The measured efficiency profiles show a gradually decreasing distribution from the central region to the outermost regions of the FZP patterns, which realises Gaussian beam optics. Larger correcting efficiencies than the theoretical values of conventional FZPs were observed. A-FZPs also enable the technical difficulties at higher spatial resolution to be reduced and for higher efficiency X-ray imaging.

Acknowledgements

The authors thank Tomoki Fukui for technical support. The experiments were performed at the BL20XU beamline at SPring-8 under the approval of the Japan Synchrotron Radiation Institute (JASRI) (Proposal Nos. 2014B1153 and 2015B1399..

References

Cao, Q. & Jahns, J. (2003). *J. Opt. Soc. Am. A*, **20**, 1576–1581.
Chao, K., Fischer, P., Tyliszczak, T., Rekawa, S., Anderson, E. & Naulleau, P. (2012). *Opt. Express*, **20**, 9777–9783.
Chen, T., Chen, Y., Wang, C., Kempson, I., Lee, W., Chu, Y., Hwu, Y. & Margaritondo, G. (2011). *Opt. Express*, **19**, 19919–19924.
Döring, F., Robisch, A. L., Eberl, C., Osterhoff, M., Ruhlandt, A., Liese, T., Schlenkrich, F., Hoffmann, S., Bartels, M., Salditt, T. & Krebs, H. U. (2013). *Opt. Express*, **21**, 19311–19323.

Khakurel, K., Kimura, T., Joti, Y., Matsuyama, S., Yamauchi, K. & Nishino, Y. (2015). *Opt. Express*, **23**, 28182–28190.
Kimura, T., Matsuyama, S., Yamauchi, K. & Nishino, Y. (2013). *Opt. Express*, **21**, 9267–9276.
Kipp, L., Skibowski, M., Johnson, R. L., Berndt, R., Adelung, R., Harm, S. & Seemann, R. (2001). *Nature (London)*, **414**, 184–188.
Mizutani, R., Saiga, R., Takeuchi, A., Uesugi, K. & Suzuki, Y. (2013). *J. Struct. Biol.* **184**, 271–279.
Oda, M., Ozawa, A. & Yoshihara, H. (1993). *J. Vac. Sci. Technol. B*, **11**, 37–43.
Ozawa, A., Tamamura, T., Ishii, T., Yoshihara, H. & Kagoshima, T. (1997). *Microelectron. Eng.* **35**, 525–529.
Sekimoto, M., Ozawa, A., Ohkubo, T., Yoshihira, H., Kakuchi, M. & Tamura, T. (1998). *X-ray Microscopy II*, p. 178. Berlin: Springer.
Suzuki, Y. & Takeuchi, A. (2012). *Jpn. J. Appl. Phys.* **51**, 086701.
Suzuki, Y. & Takeuchi, A. (2010*b*). *AIP Conf. Proc.* **1234**, 453–456.
Suzuki, Y., Takeuchi, A., Takano, H., Ohigashi, T. & Takenaka, H. (2001). *Proc. SPIE*, **4499**, 74–84.
Suzuki, Y., Takeuchi, A., Takano, H. & Takenaka, H. (2005). *Jpn. J. Appl. Phys.* **44**, 1994–1998.
Suzuki, Y., Takeuchi, A., Takenaka, H. & Okada, I. (2010*a*). *X-ray Opt. Instrum.* **2010**, 824387.
Suzuki, Y., Uesugi, K., Takimoto, N., Fukui, T., Aoyama, K., Takeuchi, A., Takano, H., Yagi, N., Mochizuki, T., Goto, S., Takeshita, K., Takahashi, S., Ohashi, H., Furukawa, Y., Ohata, T., Matsushita, T., Ishizawa, Y., Yamazaki, H., Yabashi, M., Tanaka, T., Kitamura, H. & Ishikawa, T. (2004). *AIP Conf. Proc.* **706**, 344–347.
Takano, H., Tsuji, T., Hashimoto, T., Koyama, T., Tsusaka, Y. & Kagoshima, Y. (2010). *Appl. Phys. Expr.* **3**, 076702.
Takeuchi, A., Suzuki, Y. & Uesugi, K. (2012). *Rev. Sci. Instrum.* **83**, 083701.
Takeuchi, A., Suzuki, Y. & Uesugi, K. (2015). *Jpn. J. Appl. Phys.* **54**, 092401.
Takeuchi, A., Uesugi, K. & Suzuki, Y. (2013). *J. Synchrotron Rad.* **20**, 793–800.
Takeuchi, A., Uesugi, K., Suzuki, Y. & Siu, K. K. W. (2010). *AIP Conf. Proc.* **1266**, 42–46.
Takeuchi, A., Uesugi, K., Suzuki, Y., Tamura, S. & Kamijo, N. (2006). *IPAP Conf.* **7**, 360–362.
Takeuchi, A., Uesugi, K., Takano, H. & Suzuki, Y. (2002). *Rev. Sci. Instrum.* **73**, 4246–4249.
Toda, H., Uesugi, K., Takeuchi, A., Minami, K., Kobayashi, M. & Kobayashi, T. (2006). *Appl. Phys. Lett.* **89**, 143112.
Tsuchiyama, A., Uesugi, M., Matsushima, T., Michikami, T., Kadono, T., Nakamura, T., Uesugi, K., Nakano, T., Sandford, S. A., Noguchi, R., Matsumoto, T., Matsuno, J., Nagano, T., Imai, Y., Takeuchi, A., Suzuki, Y., Ogami, T., Katagiri, J., Ebihara, M., Ireland, T. R., Kitajima, F., Nagao, K., Naraoka, H., Noguchi, T., Okazaki, R., Yurimoto, H., Zolensky, M. E., Mukai, T., Abe, M., Yada, T., Fujimura, A., Yoshikawa, M. & Kawaguchi, J. (2011). *Science*, **333**, 1125–1128.
Uesugi, K., Takeuchi, A. & Suzuki, Y. (2006). *Proc. SPIE*, **6318**, 63181F.
Yang, B. X. (1993). *Nucl. Instrum. Methods Phys. Res. A*, **328**, 578–587.